



OPEN ACCESS

EDITED BY

Weimin Huang,
Memorial University of Newfoundland,
Canada

REVIEWED BY

Xin Qiao,
Memorial University of Newfoundland,
Canada
Guanchun Wang,
Xidian University, China
Jiaxin Li,
Chinese Academy of Sciences (CAS), China

*CORRESPONDENCE

Kun Gao
✉ gaokun@bit.edu.cn

RECEIVED 12 June 2024

ACCEPTED 15 July 2024

PUBLISHED 21 August 2024

CITATION

Zhao X, Gao K, Huang F, Chen J, Xiong Z,
Song L and Lv M (2024) Tensor adaptive
reconstruction cascaded with spatial-spectral
fusion for marine target detection.
Front. Mar. Sci. 11:1447189.
doi: 10.3389/fmars.2024.1447189

COPYRIGHT

© 2024 Zhao, Gao, Huang, Chen, Xiong, Song
and Lv. This is an open-access article
distributed under the terms of the [Creative
Commons Attribution License \(CC BY\)](https://creativecommons.org/licenses/by/4.0/). The
use, distribution or reproduction in other
forums is permitted, provided the original
author(s) and the copyright owner(s) are
credited and that the original publication in
this journal is cited, in accordance with
accepted academic practice. No use,
distribution or reproduction is permitted
which does not comply with these terms.

Tensor adaptive reconstruction cascaded with spatial-spectral fusion for marine target detection

Xiaobin Zhao¹, Kun Gao^{1*}, Fenghua Huang², Junqi Chen³,
Zhangxi Xiong³, Lujie Song³ and Ming Lv⁴

¹School of Optics and Photonics, Beijing Institute of Technology, Beijing, China, ²Fujian Key Laboratory of Spatial Information Perception and Intelligent Processing, Yango University, Fuzhou, China, ³School of Information and Electronics, Beijing Institute of Technology, Beijing, China, ⁴School of Computer Science and Technology, Xinjiang University, Urumqi, China

Hyperspectral target detection has a wide range of applications in marine target monitoring. Traditional methods for target detection take less consideration of the inherent structural information of hyperspectral images and make insufficient use of spatial information. These algorithms may experience degradation in efficacy during complex scenarios. To address these issues, this study introduces a hyperspectral target detection approach based on tensor adaptive reconstruction cascade spatial-spectral fusion, named as TRSSF. First, the position of the pixel that best matches the prior spectrum is obtained. Second, tensor decomposition and reconstruction of the original hyperspectral data are performed. Linear total variation smoothing is used to acquire the principal components in the spatial dimensionality unfolding of data, and correlation regularization robust principal component analysis is employed to derive the spectral dimensionality unfolding's principal components of data. Finally, the spatial-spectral fusion method is proposed for detecting hyperspectral targets on the reconstructed data. The use of multi-morphological feature fusion can fully utilize the spatial features to complement the spectral detection results and improve the integrity of target detection. The experiments conducted on the publicly available dataset and collected datasets demonstrated the effective detection achieved by the proposed method.

KEYWORDS

marine target monitoring, hyperspectral target detection, tensor adaptive reconstruction, robust principal component analysis, spatial-spectral fusion

1 Introduction

The transport, distribution, and accumulation of marine targets, such as oil pollution and wake (as shown in Figure 1), have a significant detrimental effect on marine ecosystems. Hyperspectral imaging (HSI) offers the advantage of abundant spectral information, enabling the differentiation of marine targets of similar shapes and sizes but varying materials (Zou and Shi, 2015; Sun et al., 2024a). As hyperspectral remote sensing has advanced, hyperspectral image super-resolution (Li et al., 2022a, 2023a, b, 2024) and target detection technology have become increasingly important. Of these, target detection technology has found extensive applications in civilian and military domains (Nasrabadi, 2013; Hou et al., 2022; Wang et al., 2024). In the civilian field, the technology can be used in plant disease detection, insect pest detection, mineral detection, medical detection, etc. In the military field, it can be used in landmine detection, sea target detection, and ground camouflage hidden target detection (Coorey, 2018; Wang et al., 2023).

As hyperspectral technology has progressed, numerous traditional strategies for hyperspectral imagery target detection have long been formed (Chen et al., 2011; Li and Du, 2016; Liu et al., 2021a). Hyperspectral target detection methods are categorized based on the amount of information fed into spectral-based, spatial-spectral, and deep feature extraction methods (Du and Zhang, 2010; Zhao et al., 2020c; Hou et al., 2021; Gao et al., 2023). Numerous hyperspectral target detection approaches rely on spectral domain data. The constrained energy minimization (CEM) technique devises a filter capable of minimizing information output while adhering to constraints imposed by the prior target spectrum (Farrand and Harsanyi, 1997). Spectral angle mapper (Kruse et al., 1993) can detect the targets without information distribution assumptions and is considered one of the most straightforward detection mechanisms. Spectral matching filter (MF) (Manolakis et al., 2009) defines target detection as a hypothetical test and has good detection performance in a simple background. Orthogonal subspace projection is a subspace model detection algorithm in a linear mixed model (Harsanyi and Chang, 1994). Adaptive cosine

estimation is a probability statistical algorithm that employs various techniques to extend detection statistics, improving the differentiation between the target and the background (Manolakis et al., 2003). Spectral information divergence calculates the information divergence between two spectrums (Chang, 1999). Lin et al. proposed a multi-target band selection method for hyperspectral target detection, based on an ideal solution optimization strategy (MOBS), with the aim of selecting bands with greater target separation and stronger robustness for different application scenarios (Sun et al., 2024b).

With the increase in spatial information in hyperspectral images, hyperspectral target detection methods that integrate spatial and spectral information have emerged (Wei et al., 2019). Yang and Shi (2016) proposed a method that uses a target pixel to execute target detection and total variation to smooth the space of an image. Zhao et al. (2021b) designed a fractional adaptive CEM. The initial data is processed with fractional Fourier, and then a locally CEM is used for target acquisition. Gao et al. introduced the tree-structured encoding approach to locate targets in hyperspectral data (Sun et al., 2020). Yang et al. introduced the sparse spatial constraint energy minimization (Yang et al., 2019; Zhao et al., 2020b). Sun et al. proposed an information entropy estimation target detection method based on point set topology. The method consists of constructing a parallel topological space to sort the raw HSI data and introducing information entropy estimation in combination with *a priori* information about the target (Sun et al., 2024c).

In the realm of adopting deep feature algorithms, Zhang et al. presented a hyperspectral target detection neural network, which uses deep features (Li and Du, 2016; Zhang et al., 2020). The novel deep spatial-spectral network was developed by Shi et al. as an unsupervised detection means. This network incorporates a typical detector and an edge-preserving filter to identify targets (Shi et al., 2020). Generally, traditional methods often overlook the inherent structural characteristics of hyperspectral data and underutilize spatial information. Dong et al. presented a lightweight convolutional neural network (LCNN) (Dong et al., 2023) for reducing computational complexity. In deep learning approaches, the limited samples pose challenges in training deep networks.

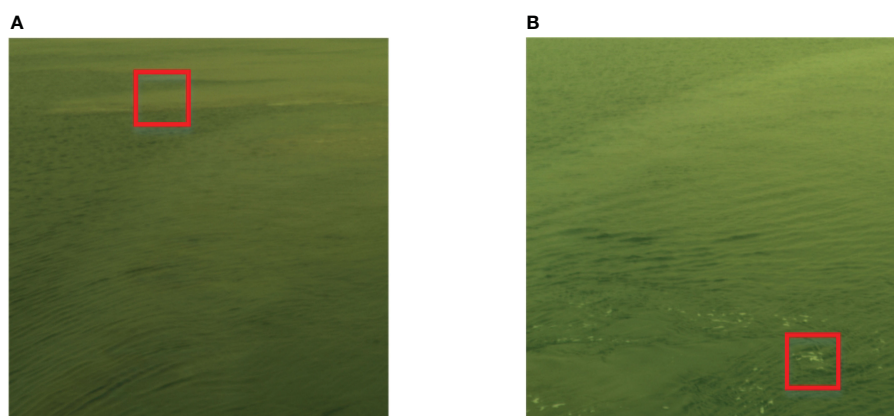


FIGURE 1
Water surface oil pollution (A) and wake (B).

In recent years, some new methods of using tensors have attracted the interest of researchers. Tensor extends the concepts of vectors and matrices to accommodate higher-order data so that multidimensional datasets can be treated as a whole. Tensor representation can provide a convenient and accurate strategy for capturing the interrelationship between multiple dimensions (Kolda and Bader, 2009). HSI encompasses both spatial and spectral dimensions, thus is recognized as a third-order data cube (Zhao et al., 2021a). The tensor representation technique has found applications in various hyperspectral image processing tasks, such as the noise reduction algorithm (Renard and Bourennane, 2008; Guo et al., 2013; Liu et al., 2021b), unmixing algorithm (Veganzones et al., 2015), and classification algorithm (Renard and Bourennane, 2009).

There are few studies using the tensor representation method for hyperspectral target detection. Chen et al. introduced the technique called tensor principal component analysis through Fourier transform (TRPCAF), which considers the hyperspectrum, including principal components and residuals (Chen et al., 2018; Chen and Wang, 2019). Li et al. introduced the prior tensor approximation (PTA) technique to detect anomalies in hyperspectral images (Li et al., 2020; Feng et al., 2021). Gu et al. introduced tensor matched subspace detector (TMSD) (Liu et al., 2016). Zhao introduced a hyperspectral target detection algorithm employing dictionary learning, leveraging Tucker tensor decomposition (TTDL) (Cai et al., 2010; Zhao et al., 2020a). Chen et al. proposed a spectral graph contrast clustering assignment and the spectral graph transformer method for hyperspectral target detection. This method includes constructing pixel spectra into spectral graphs and proposing a new spectral graph comparison cluster allocation method for providing the model with good spectral recognition ability (Chen et al., 2024). Dong et al. developed a novel deep space-spectral joint sparse prior coding network. This network skillfully integrates the domain knowledge of hyperspectral target detection into the neural network and has clear interpretability (Dong et al., 2024). However, these methods cannot choose the appropriate principal components in tensor decomposition and reconstruction and do not fully use spatial information. Hence, this study introduces a hyperspectral target detection method termed tensor adaptive reconstruction cascade spatial-spectral fusion (TRSSF). The primary contributions of this study include:

1. A tensor adaptive reconstruction cascade spatial-spectral fusion model is proposed. The model not only extracts intrinsic features of the target background spectrum to increase its discriminatory capability but also maximizes the use of spatial-spectral information to increase target detection rates. The maximum improvement in detection rates over the four datasets ranged from 32% to 81% compared with the state-of-the-art method.
2. The linear total variation is employed in the matrix processing of unfolding hyperspectral spatial dimensions, mitigating noise effects and increasing the accuracy of decomposing sparse and low-rank matrices. When analyzing the principal components of hyperspectral

spectral dimension unfolding matrices, correlation regularization can bring the data target spectra closer to the prior spectra.

3. Adaptive CEM and similarity multiple morphological profile strategies are used in the spatial-spectral fusion approach. In these techniques, the use of multiple morphological feature fusion allows for the combined use of spatial features to complement the spectral detection results, thereby improving the overall target detection integrity.

This article is structured as follows. Section 1 constitutes the introduction, which mainly introduces the research background, research methods, and contributions of the study. Section 2 introduces the proposed hyperspectral target detection framework based on the tensor adaptive reconstruction cascade spatial-spectral fusion strategy in detail. Section 3 details the experimental results as well as analysis conducted on four hyperspectral datasets. Section 4 contains the conclusion of the study.

2 Proposed target detection method

The framework of the proposed TRSSF is depicted in Figure 2. First, the MF is used to obtain the position of the most similar target to the prior target spectrum within the image. Second, the tensor decomposition and adaptive reconstruction approach is introduced for the original hyperspectral data with the aim of deriving the principal components of the hyperspectral spatial and spectral dimensions (Dian et al., 2017; Zhao et al., 2023). For the spatial orientation, linear total variation is used to process the data, and the robust principal component technique is used to obtain the principal components. In the spectral dimension, the robust principal component method with the prior and measured spectrum's smallest energy difference is used to obtain the principal components. After obtaining the principal components, the data are restructured. Finally, to take full advantage of the spatial and spectral features, a novel spatial-spectral fusion method is proposed.

2.1 Most similar target position acquisition

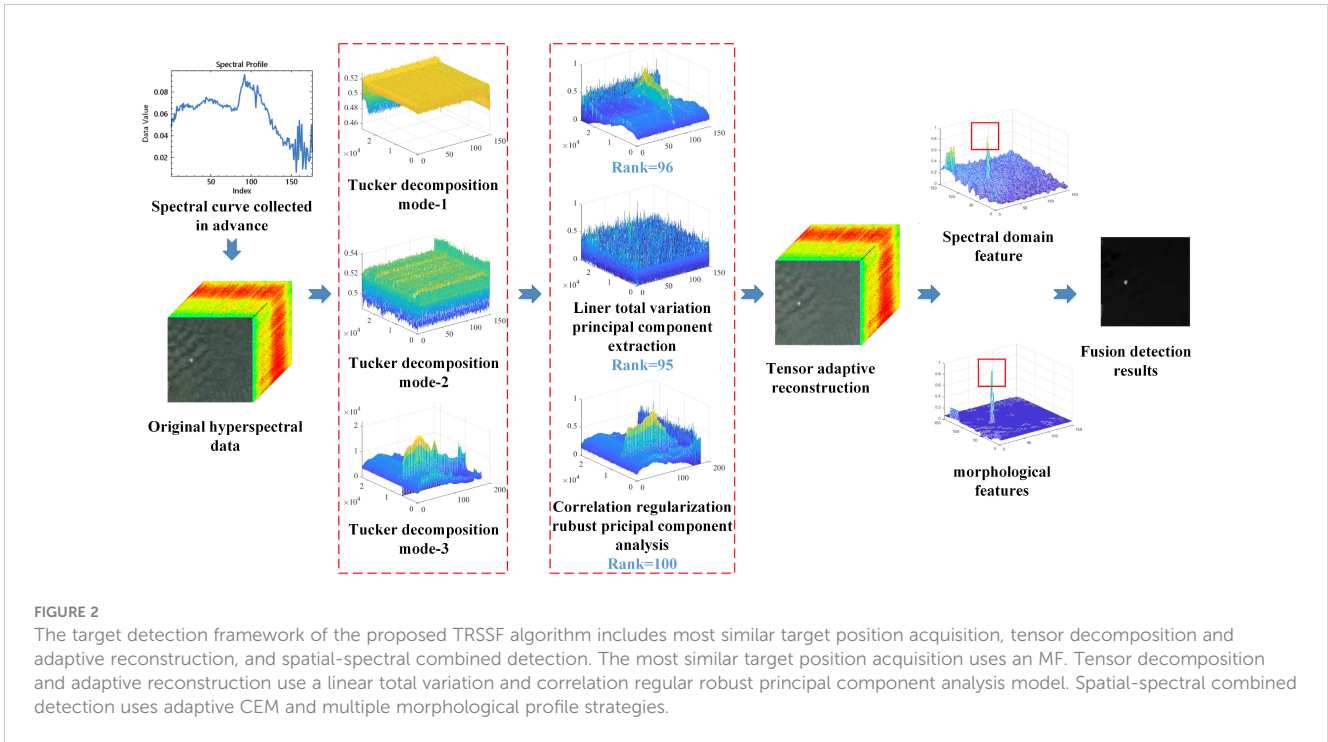
The matched filter is employed to locate similar target pixels in images (DiPietro et al., 2012). The likelihood ratio $\Lambda(\mathbf{h})$ is determined by the Equation 1:

$$\Lambda(\mathbf{h}) = \frac{p(\mathbf{h}|\text{Tp})}{p(\mathbf{h}|\text{Ta})}, \quad (1)$$

where Tp means target present and Ta means target absent. If $\Lambda(\mathbf{h})$ exceeds the threshold, Tp is accepted, otherwise, Ta is accepted.

The probability density function follows a normal distribution model, which is expressed as Equation 2:

$$\begin{aligned} H_0 : \mathbf{h} &\sim N(\mathbf{u}_b, \Sigma_b) \text{ Ta} \\ H_1 : \mathbf{h} &\sim N(\mathbf{u}_t, \Sigma_t) \text{ Tp,} \end{aligned} \quad (2)$$



where u_b and u_t are the mean of the target and background, respectively. Σ_b and Σ_t represent the covariance matrix of the target and background, respectively. The matched filter based on background statistics is as Equation 3 (Akhter et al., 2014):

$$r_{MF}(h) = \frac{(t - u_t)^T \Sigma_b^{-1} (h - u_b)}{(t - u_t)^T \Sigma_b^{-1} (t - u_t)}, \quad (3)$$

where t denotes the prior spectrum, h denotes the pixel-tested spectrum, and Σ_b^{-1} refers to the background matrix inversion operation.

Based on the similarity obtained, the target with the highest degree of similarity to the prior information is selected to obtain the target's position within the image. The spectrum of the reconstruction data in this position is used as follow-up prior spectrum. The formula is as Equation 4:

$$po = find(r_{MF} == max(r_{MF})), \quad (4)$$

where po is the position of the subsequent need.

2.2 Tensor decomposition and adaptive reconstruction of the hyperspectral data

In Figure 3, the hyperspectral image along with the expansion's singular value distributions for modes 1, 2, and 3 are displayed. The rapid convergence of the curves shows that each mode's decomposition possesses a low rank. The low rank characteristic can apply to hyperspectral tensor adaptive reconstruction.

2.2.1 Decomposition of the tensor using Tucker decomposition

The hyperspectral image is represented as the tensor $\mathcal{D} \in \mathbb{R}^{T_1 \times T_2 \times T_3}$, where T_1 , T_2 and T_3 represent the row, column, and

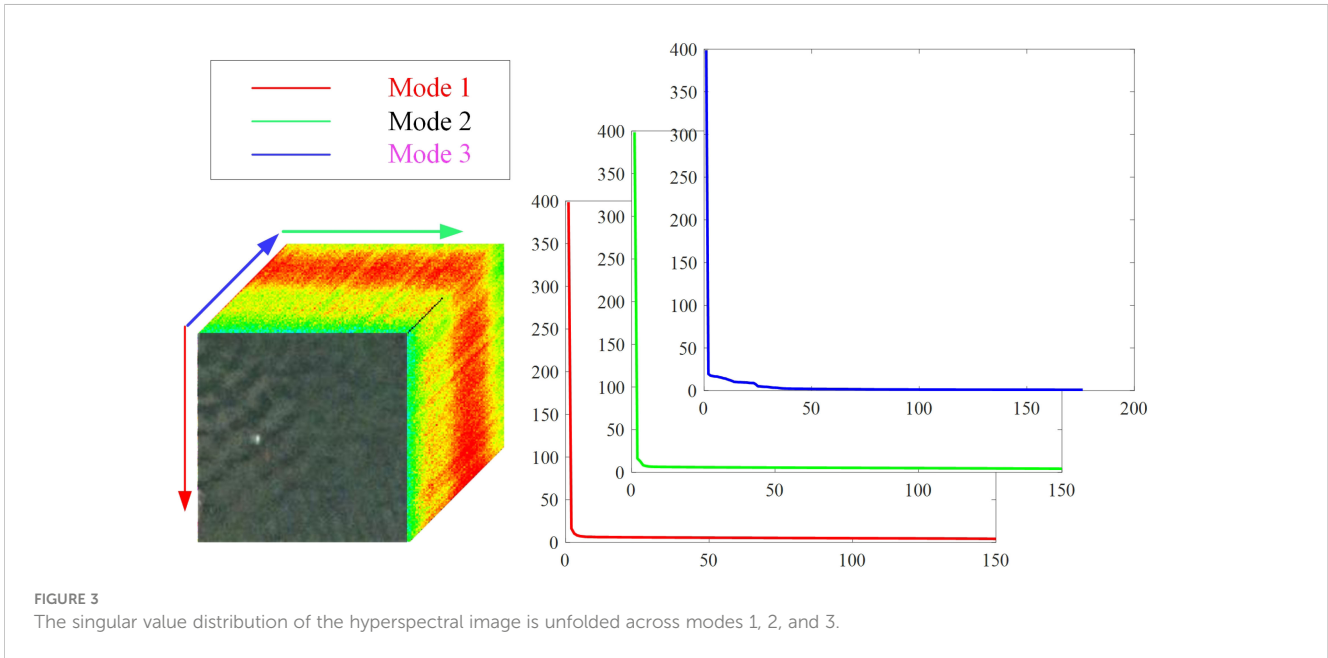
band, respectively (Hou et al., 2021). Owing to the influence of several factors (topography, illumination, etc.), there are certain differences in the target spectral curve in the complex background. Tucker decomposition can effectively preserve the three-dimensional structural details of the data and eliminate other impurity signals, which is essential for the background complex hyperspectral images. They provide simple compression to maintain the principal components of the different factor matrices, thus increasing the distinction between target and background in complex background images. Therefore, Tucker decomposition and reconstruction of hyperspectral datasets is performed to obtain more stable feature-enhanced target and background separability. The Tucker decomposition formula is as Equation 5:

$$\mathcal{D} \approx \mathcal{G} \times_1 \mathbf{P} \times_2 \mathbf{Q} \times_3 \mathbf{W}, \quad (5)$$

where $\mathcal{G} \in \mathbb{R}^{T_1 \times T_2 \times T_3}$ denotes the core tensor, signifying the degree of interaction among distinct components $\mathbf{P} \in \mathbb{R}^{T_2 \times T_3 \times T_1}$, $\mathbf{Q} \in \mathbb{R}^{T_1 \times T_3 \times T_2}$ and $\mathbf{W} \in \mathbb{R}^{T_1 \times T_2 \times T_3}$ denote three factor matrices. They are the principal components for each mode. It is optimized as Equation 6:

$$\begin{aligned} & \arg \min_{\mathcal{G}, \mathbf{P}, \mathbf{Q}, \mathbf{W}} \|\mathcal{D} - \mathcal{G} \times_1 \mathbf{P} \times_2 \mathbf{Q} \times_3 \mathbf{W}\|_2 \\ & \text{s. t. } \begin{cases} \mathcal{G} \in \mathbb{R}^{T_1 \times T_2 \times T_3} \\ \mathbf{P} \in \mathbb{R}^{T_2 \times T_3 \times T_1}, \mathbf{Q} \in \mathbb{R}^{T_1 \times T_3 \times T_2}, \mathbf{W} \in \mathbb{R}^{T_1 \times T_2 \times T_3} \\ \mathbf{P}^T \mathbf{P} = \mathbf{I}_1, \mathbf{Q}^T \mathbf{Q} = \mathbf{I}_2, \mathbf{W}^T \mathbf{W} = \mathbf{I}_3 \end{cases} \end{aligned} \quad (6)$$

The equation above is typically solved using the alternating least squares method. When the two matrices remain constant, an additional factor matrix is acquired through characteristic value decomposition.



2.2.2 Linear total variation smoothing robust principal component analysis

Tucker decomposition provides a simple compression method and can retain the most important information (Li et al., 2018; Xu et al., 2019). Because each factor matrix has different eigenvalues, their capacity to capture significant information also varies. Determining the appropriate numbers for r_i (i is 1, 2, 3) is crucial for distinct factor matrices (P, Q, W).

To mitigate the influence of noise on principal component extraction, this article applies total variation processing to the spatial dimension of the hyperspectral data. Total variation is defined as the difference between adjacent pixels (He et al., 2015). The total variation formula is as Equation 7:

$$V(i, j) = \begin{cases} V(i + 1, j) - V(i, j) & \text{if } i < m \\ V(1, j) - V(i, j) & \text{if } i = m \end{cases}, \quad (7)$$

where m denotes the number of columns of V . The total variation formula of P is as Equation 8:

$$P_{TV}(i, j) = \begin{cases} P(i, j + 1) - P(i, j), & \text{if } j < T_1 \\ P(i, 1) - P(i, j), & \text{if } j = T_1 \end{cases}. \quad (8)$$

The total variation formula of Q is as Equation 9:

$$Q_{TV}(i, j) = \begin{cases} Q(i, j + 1) - Q(i, j), & \text{if } j < T_2 \\ Q(i, 1) - Q(i, j), & \text{if } j = T_2 \end{cases}. \quad (9)$$

In the hyperspectral image, the background components are highly correlated; therefore, it is considered low rank. After the spatial dimension is smoothed, the robust principal component analysis method (RPCA) is used to acquire the data's rank. Its formula is as Equation 10:

$$\begin{aligned} \min_{T, M} \text{rank}(M) + \lambda \|T\|_0 \\ \text{s.t. } M + T = X, \end{aligned} \quad (10)$$

where $M \in \mathbb{R}^{T_1 T_3 \times T_2}$ represents the low rank matrix, $T \in \mathbb{R}^{T_1 T_3 \times T_2}$ represents the sparse matrix, $X \in \mathbb{R}^{T_1 T_3 \times T_2}$ represents the unfolding of the original data, and λ denotes a positive parameter regulating sparsity. Relaxing Equation 10 yields a manageable optimization problem. The L_1 norm is used to replace the L_0 norm, while the nuclear norm is used to replace the rank. It can transform into solving the Equation 11:

$$\begin{aligned} \min_{T, M} \|M\|_* + \lambda \|T\|_1 \\ \text{s.t. } M + T = X. \end{aligned} \quad (11)$$

The original RPCA work in Candès et al. (2011) introduced an iterative thresholding method of low complexity with poor convergence. The alternating direction method of multipliers strategy is extensively used in optimization problems, which has good convergence (Kang et al., 2015). Therefore, it is adopted to solve this issue. It is as Equation 12:

$$\begin{aligned} L(M, T, Y, \mu) &= \|M\|_* + \lambda \|T\|_1 + \langle Y, X - M - T \rangle \\ &+ \frac{\mu}{2} \|X - M - T\|_F^2 \\ &= \|M\|_* + \lambda \|T\|_1 + \frac{\mu}{2} \|X - M - T + \frac{Y}{\mu}\|_F^2 - \frac{1}{2\mu} \|Y\|_F^2, \end{aligned} \quad (12)$$

where Y denotes the Lagrangian multiplier matrix, μ denotes the positive penalty scalar, $\langle \cdot, \cdot \rangle$ is the inner product, and $\|\cdot\|_F^2$ signifies the Frobenius norm. The adopted algorithm involves updating the variables M, T and Y by minimizing function L while keeping the other variables fixed.

(1) Updating M_k : when other parameters are fixed, M_k is obtained by solving the Equations 13 and 14:

$$M_{k+1} \leftarrow \arg \min_A \frac{1}{\mu} \left\| M \right\|_k + \frac{1}{2} \left\| X - M - T_k + \frac{Y_1}{\mu} \right\|_F^2, \quad (13)$$

$$M_{k+1} = \Theta_{\mu_k^{-1}}(X - T_k + \mu_k^{-1} Y_k), \quad (14)$$

where Θ denotes the singular value threshold operator and k is the number of iterations.

(2) Updating T_k : when other parameters are fixed, T_k is obtained by solving the Equations 15 and 16:

$$T_{k+1} \leftarrow \arg \min_E \frac{\lambda}{2\mu} \| T \|_1 + \frac{1}{2} \| X - M_{k+1} + \frac{Y_1}{\mu} \|_F^2, \quad (15)$$

$$T_{k+1} = S_{\lambda\mu_k^{-1}}[X - M_{k+1} + \mu_k^{-1} Y_k], \quad (16)$$

where $S_{\lambda\mu_k^{-1}}$ is the shrinkage operator (He et al., 2011); it is expressed as Equation 17:

$$S_{\mathcal{E}}(\mathbf{x}) = \text{sgn}(\mathbf{x}) \max(|\mathbf{x}| - \mathcal{E}, 0). \quad (17)$$

(3) Updating Y_k and μ_k : they are obtained by solving the Equations 18 and 19:

$$Y_{k+1} = Y_k + \mu_k(X - M_{k+1} - T_{k+1}), \quad (18)$$

$$\mu_{k+1} = \rho\mu_k. \quad (19)$$

By solving the above formula, the low rank matrix M (\hat{P} or \hat{Q}) is acquired. The appropriate rank of the matrix is adaptively obtained. The outlined workflow is encapsulated in Algorithm 1.

2.2.3 Correlation regular robust principal component analysis

In the direction of expansion along a spectral dimension, to obtain the target that is closer to the prior spectrum, the minimum regular constraint for the tested and prior spectrums' difference is added to the RPCA. It is as Equation 20:

$$\min_{M,T} \left\| M \right\|_* + \lambda \left\| T \right\|_1 + \beta \left\| H \odot T - D \right\|_F \quad (20)$$

s. t. $M + T = X,$

Input: Data matrix \mathcal{X} (\mathcal{P} or \mathcal{Q}), $\lambda > 0$

Output: The optimal solution \mathcal{M} (\hat{P} or \hat{Q})

- 1: **Initialize:** $M_0 = T_0 = 0, Y = X/\max(\|X\|_2, \lambda^{-1}\|X\|_\infty), \mu_0 = 1.25/\|X\|_2, \mu_{\max} = \mu_0 10^7, k=0, tol=10^{-7}$
- 2: The \mathcal{P} is processed using Equation 8;
- 3: The \mathcal{Q} is processed using Equation 9;
- 4: **while** $\|X - M_k - T_k\|_F / \|X\|_F < tol$ **do**
- 5: Compute variable M_{k+1} using Equation 14;
- 6: Compute variable T_{k+1} using Equation 16;
- 7: Compute variable \mathcal{Y} using Equation 18;
- 8: Compute variable μ using Equation 19;

- 9: $k \leftarrow k + 1;$
- 10: **end while**

Algorithm 1. The linear total variation smoothing framework.

where \odot is the Hardman product, H is the spectral all-one matrix of the prior position, and D is the prior spectral matrix. The formula is displaced as Equation 21:

$$\min_{M,T} \|M\|_* + \lambda \|T\|_1 + \beta \|H \odot U - D\|_F^2 \quad (21)$$

s. t. $M + T = X, U = T.$

The augmented Lagrangian function is as Equation 22:

$$\begin{aligned} L(M, T, U, Y_1, Y_2) &= \|M\|_* + \lambda \|T\|_1 + \beta \|H \odot U - D\|_F^2 \\ &+ \langle Y_1, X - M - T \rangle + \langle Y_2, T - U \rangle \\ &+ \frac{\mu}{2} (\|X - M - T\|_F^2 + \|T - U\|_F^2) \\ &= \|M\|_* + \lambda \|T\|_1 + \beta \|H \odot U - D\|_F^2 \\ &- \frac{\mu}{2\mu} (\|Y_1\|_F^2 + \|Y_2\|_F^2) \\ &+ \frac{\mu}{2} \left(\left\| X - M - T + \frac{Y_1}{\mu} \right\|_F^2 + \left\| T - U + \frac{Y_2}{\mu} \right\|_F^2 \right) \end{aligned} \quad (22)$$

where Y_1 and Y_2 are the Lagrangian multiplier matrices, β and μ are the positive penalty scalar, $\|\cdot\|_F^2$ symbolizes the Frobenius norm, and $\langle \cdot, \cdot \rangle$ denotes the inner product. The solution involves updating the variables M, T, U, Y_1 and Y_2 by minimizing L while keeping other variables fixed.

(1) Updating M_k : when other variables are fixed, M_k is obtained by computing the Equations 23 and 24:

$$M_{k+1} \leftarrow \arg \min \frac{1}{\mu} \left\| M \right\|_* + \frac{1}{2} \left\| X - M - T_k + \frac{Y_1}{\mu} \right\|_F^2, \quad (23)$$

$$M_{k+1} = \Theta(X - T_k + \mu_k^{-1} Y_k). \quad (24)$$

(2) Updating T_k : when other parameters are fixed, T_k is obtained by solving the Equations 25 and 26:

$$T_{K+1} \leftarrow \arg \min \frac{\lambda}{2\mu} \| T \|_1 + \frac{1}{2} \left\| T - \frac{1}{2} \left(U_K - \frac{Y_2}{\mu} + X - M_{K+1} + \frac{Y_1}{\mu} \right) \right\|_F^2, \quad (25)$$

$$T_{k+1} = S_{\lambda/(2\mu)} \left[\frac{1}{2} \left(U_K - \frac{Y_2}{\mu} + X - M_{K+1} + \frac{Y_1}{\mu} \right) \right]. \quad (26)$$

(3) Updating U_k : when other parameters are fixed, U_k is obtained by solving the Equations 27 and 28:

$$U_{k+1} \leftarrow \arg \min_U \frac{\beta}{\mu} \| H \odot U - D \|_F^2 + \frac{1}{2} \left\| U - T_{k+1} - \frac{Y_2}{\mu} \right\|_F^2, \quad (27)$$

$$U_{k+1} = \left(\frac{1}{H + O} \right) \odot \left(D + T_{k+1} + \frac{Y_2}{\mu} \right), \quad (28)$$

where O is a matrix of all ones.

(4) Updating Y_1, Y_2 and μ_k : Y_k and μ_k are obtained by solving the Equations 29–31:

$$Y_1 \leftarrow Y_1 + \mu_k (X - M_{k+1} - T_{k+1}), \tag{29}$$

$$Y_2 \leftarrow Y_2 + \mu_k (T_{k+1} - U_{k+1}), \tag{30}$$

$$\mu_{k+1} = \rho \mu_k. \tag{31}$$

By solving the above formula, the low-rank variable $U(\hat{W})$ is obtained, and the appropriate rank of the matrix is adaptively obtained. The outlined method is summarized in Algorithm 2.

Input: The spectral imagery $X(W)$, parameters $\lambda > 0, \beta > 0$ **Output:** The optimal solution $\mathcal{M}(\hat{W})$

- 1: **Initialize:** $M_0 = T_0 = U_0 = 0, Y_1 = X / \max(\|X\|_2, \lambda^{-1} \|X\|_\infty), Y_2 = 0, \mu_0 = 1.25 / \|X\|_2, \mu_{\max} = \mu_0 10^7, k = 0, tol_1 = 10^{-7}, tol_2 = 10^{-3}$
- 2: **while** $\|X - M_k - T_k\|_F / \|X\|_F < tol$ **do**
- 3: Compute variable M_{k+1} using Equation 24;
- 4: Compute variable T_{k+1} using Equation 26;
- 5: Compute variable U_{k+1} using Equation 28;
- 6: Compute variable Y_1 using Equation 29;
- 7: Compute variable Y_2 using Equation 30;
- 8: Compute variable μ_{k+1} using Equation 31;
- 9: $k \leftarrow k + 1$;
- 10: **end while**

Algorithm 2. The framework of correlation regular robust principal component analysis.

In the adaptive acquisition of the rank (r_1, r_2 and r_3) of the three factor matrices, tensor restoration is used to recover the hyperspectral three-dimensional images in which it is easy to detect the target. The reconstructed data have the same spectral dimension and are calculated as Equation 32:

$$\tilde{D} \approx \mathcal{G}_r \times_1 P_{r_1} \times_2 Q_{r_2} \times_3 W_{r_3}, \tag{32}$$

where $P_{r_1} = P(:, 1:r_1), Q_{r_2} = Q(:, 1:r_2), W_{r_3} = W(:, 1:r_3)$ and $\mathcal{G}_r = \mathcal{G}(1:r_1, 1:r_2, 1:r_3)$.

The r_i ($i \in 1, 2, 3$) signifies the count of principal components in distinct factor matrices.

The intrinsic features of the hyperspectral image can be effectively retained by tensors. In Figure 4, spectral curves of a randomly chosen target-target, as well as target-background pixels, are presented from the pollution dataset before and after tensor reconstruction. The legend O denotes the original data spectral profile and T denotes the reconstructed data spectral profile. In the 60 to 80 band of Figure 4A, the separation between the black lines is less than the separation between the red lines. In the 60 to 80 band of Figure 4B, the separation between the black lines is greater than the separation between the red lines. This confirms that after tensor processing, the distinction between the background and target spectra is increased.

2.3 Spatial-spectral combined detection

Existing hyperspectral target detection algorithms use less spatial information. To make up for these deficiencies and improve the performance of target detection, this study adopts a spatial-spectral combined detection method for reconstruction data.

In the spectral domain, an adaptive CEM detection method is proposed. Its design needs to satisfy the Equation 33:

$$\begin{cases} \min_q q^T R q \\ q^T d = 1 \end{cases}, \tag{33}$$

where q is the filter, d denotes the prior position spectrum, and R denotes the correlation matrix. The optimal solution is as Equation 34:

$$q^* = \frac{R^{-1} d}{d^T R^{-1} d} \tag{34}$$

After derivation, the spectral domain result r_{aci} is as Equation 35:

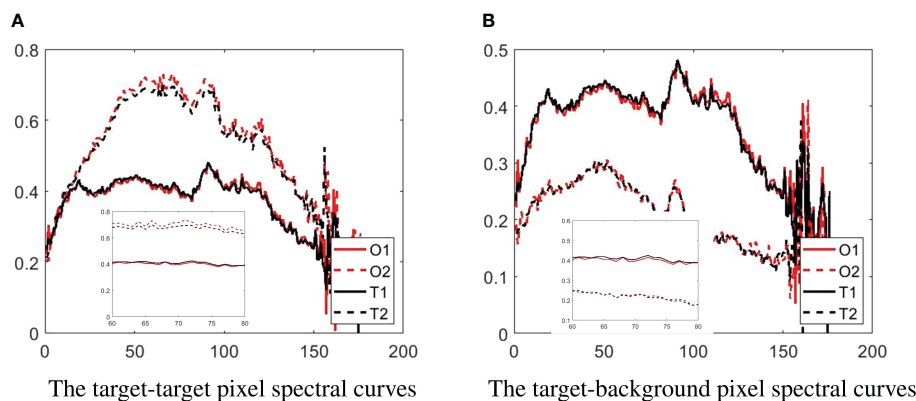


FIGURE 4 The spectral curves of target-target and target-background pixels are randomly chosen from the pollution dataset before and after Tucker decomposition and reconstruction. (A) The target-target pixel spectral curves. (B) The target-background pixel spectral curves.

$$r_{aci} = e\mathbf{q}^{*T} \mathbf{x}_i = e \frac{\mathbf{d}^T \mathbf{R}^{-1} \mathbf{x}_i}{\mathbf{d}^T \mathbf{R}^{-1} \mathbf{d}}, \quad (35)$$

where \mathbf{x}_i represents the reconstructed data's spectrum and e represents the mean of L_2 norm of the difference value between the pixels tested and its four neighborhoods.

In the spatial domain, similarity multiple morphological profile feature extraction is proposed. The similarity value is obtained by fusing the Pearson correlation coefficient with the prior spectrum's Euclidean distance from the reconstructed data using the Equation 36:

$$r_{si} = \|\mathbf{x}_i - \mathbf{d}\|_2 + \frac{cov(\mathbf{x}_i, \mathbf{d})}{\delta_{x_i} \delta_d}, \quad (36)$$

where $\|\cdot\|_2$ is the L2 norm, cov denotes the covariance, δ denotes the standard deviation, δ_{x_i} denotes the standard deviation of \mathbf{x}_i , and δ_d denotes the standard deviation of \mathbf{d} . Multiple morphological profiles obtain a multilevel representation of an image by constructing maximum and minimum trees and then using a series of attribute filtering operations, which can extract spatial, structural, and textural features in the image (Hou et al., 2021). The method has been applied in hyperspectral image classification (Aptoula et al., 2016; Bao et al., 2016). To maximize the use of spatial features for increased detection performance, the morphological feature extraction method is used to process the similarity results of the previous step. The multiple morphological profile formula adopted is as Equations 37–41:

$$\text{Area}(C) = \{\#l \mid l \in C\}, \quad (37)$$

$$\text{Height}(C) = \max_{l \in C} f(l) - \min_{l \in C} f(l), \quad (38)$$

$$\text{Volume}(C) = \sum_{l \in C} \left(\max_{l \in C} v(l) - v(l) \right), \quad (39)$$

$$\text{Diag}(C) = \sqrt{(x_{l,\max} - x_{l,\min})^2 + (y_{l,\max} - y_{l,\min})^2}, \quad (40)$$

$$\text{Std}(C) = \sqrt{\frac{1}{\text{Area}(C)} \sum_{v \in C} (f(l) - K_{\text{gray-level}}(\lambda))^2}, \quad (41)$$

where C is the connected region, $\#$ is the number of pixels in the connection area, l represents the pixel within the connected region, $f(l)$ denotes the function to obtain the value of the l pixel, and $v = \pm f, x_{l,\min}, x_{l,\max}$ and $y_{l,\min}, y_{l,\max}$ denote these extremes for the horizontal and vertical coordinates of the region that is connected, respectively. $K_{\text{gray-level}}$ denotes the average intensity of pixels within the connected region.

The multiple morphological feature fusion is as Equation 42:

$$\mathbf{R}_{\text{MMF}} = \mathbf{R}_{kk,\min} - \mathbf{R}_{ll,\max}, \quad (42)$$

where \mathbf{R}_{MMF} is the result of the fusion of multiple morphological features, $\mathbf{R}_{kk,\min}$ and $\mathbf{R}_{ll,\max}$ denote smaller pruning for attribute kk and larger pruning for attribute ll , respectively. kk and ll belong to the above five morphologies.

Figure 5 demonstrates pruning and reconstruction using multiple morphological attributes (area and height) of the maximal tree. Target features can be preserved by using the fusion of area 5 with height 1 pruning value 5 results. Therefore, targets can be extracted using this multiple morphological feature fusion.

After obtaining the spectral and spatial domain results, the spatial-spectrum fusion is realized by the Equation 43:

$$\mathbf{R} = b\mathbf{R}_{ac} + (1 - b)\mathbf{R}_{\text{MMF}}, \quad (43)$$

where b is the weighting factor, \mathbf{R}_{ac} is the result of spectral detection, and \mathbf{R}_{MMF} is the result of spatial detection. The framework of TRSSF is summarized in Algorithm 3.

Input: The spectral imagery \mathcal{X} , prior target spectrum \mathbf{d} .

Output: The result $\mathbf{R} = [r_1; \dots; r_N]$.

- 1: for $i = 1 \dots N$ do
- 2: Compute po using Equation 4;
- 3: Compute principal component of \mathcal{P} and \mathcal{Q} using Algorithm 1;
- 4: Compute principal component of \mathcal{W} using Algorithm 2;

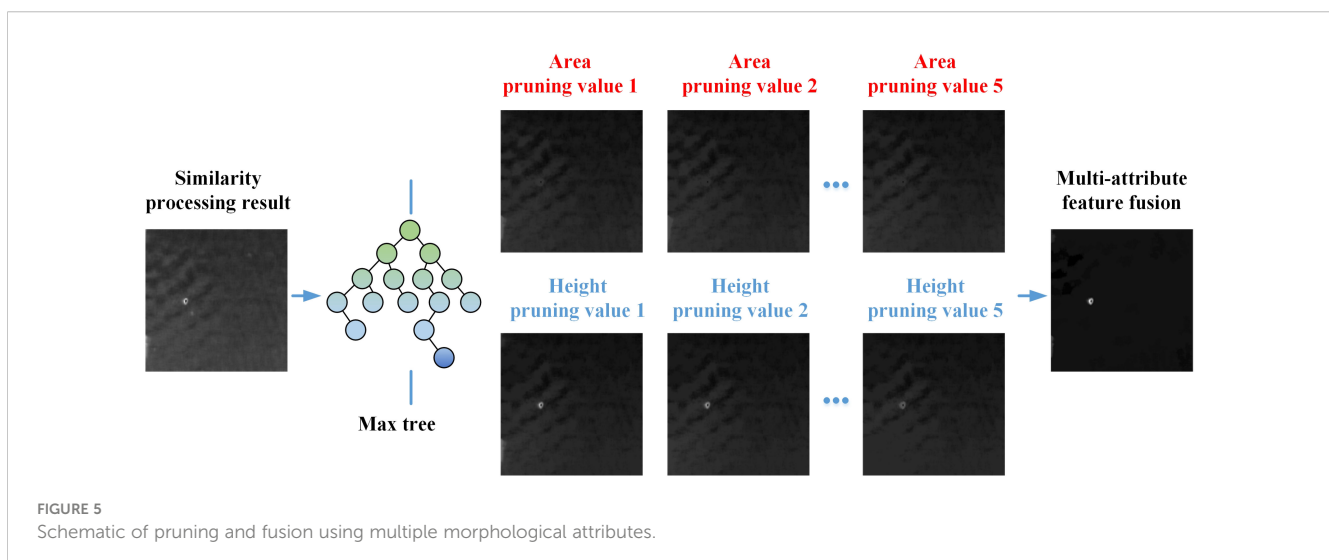


FIGURE 5 Schematic of pruning and fusion using multiple morphological attributes.

- 5: Compute \tilde{D} using Equation 32;
- 6: Compute r_{aci} using Equation 35;
- 7: Compute R_{MMF} using Equation 42;
- 8: Compute R using Equation 43;
- 9: end for

Algorithm 3. The framework of the proposed TRSSF.

Figure 6 illustrates the receiver operating characteristic curve (ROC) of the tensor adaptive reconstruct spectral feature (TS), tensor adaptive reconstruct morphological feature (TM), and proposed TRSSF. Across the four datasets, the ROCs of the proposed methods TS, TM, and TRSSF all reside near the upper left corner, indicating a strong performance for all the proposed algorithms. Out of the four images, the TRSSF algorithm’s ROC curves are closest to the upper left, indicating a superior performance for the tensor adaptive reconstructed and spatial-temporal fusion algorithm. From Table 1, it can also be observed that the spectral characteristics and morphological features have high area under the curve (AUC) values, and the spatial spectral fusion method AUC values increase very significantly.

In summary, a tensor adaptive reconstruction cascade spatial-spectral fusion algorithm is proposed for hyperspectral target detection. First, the matched filter method is adopted to acquire the position of the pixel that best matches the prior spectrum.

TABLE 1 AUC values of the tensor adaptive reconstruct spectral feature (TS), tensor adaptive reconstruct morphological feature (TM), and TRSSF on four datasets.

Image	TS	TM	TRSSF
Ship	0.9791	0.9380	0.9998
Wake	0.9774	0.9547	0.9934
Pollution	0.9972	0.9800	0.9986
Floating object	0.9294	0.9986	0.9993

Second, tensor Tucker decomposition and reconstruction by linear total variation smoothing robust principal component analysis and correlation regular robust principal component analysis are used to improve the differentiation between the target and background. Finally, the spatial-spectral fusion method is proposed to acquire the required target pixels.

3 Experiments and analysis

3.1 Hyperspectral datasets

The first data were collected by airborne HSI system SPECTIR sensors. The spatial resolution and spectral

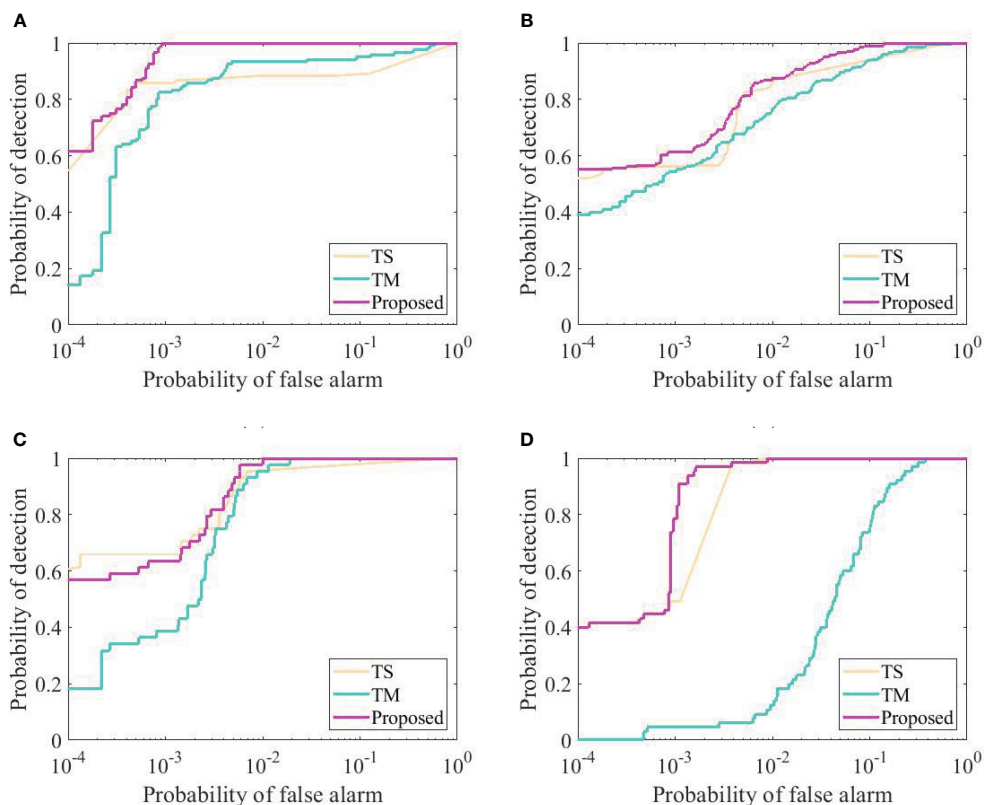


FIGURE 6 The ROC curve for different datasets. (A) Ship. (B) Wake. (C) Pollution. (D) Floating object.

resolution of the sensor were 1 m and 5 nm, respectively. The target is the ship and the background is the nearshore water (Giannandrea et al., 2013). The target spectra were obtained from the images. The detailed description of the datasets can be found in row 1 of Table 2. In addition, the false-color image (PI) and ground truth image (GT) of these datasets are displayed in rows 1 and 2 of Figures 7A, B.

The second to fourth hyperspectral datasets were collected by the Dualix spectral imaging instrument GaiaSkymini2. Its spectral range spans from 400 nm to 1,000 nm, the spatial resolution is 0.14 m, and the spectral resolution is 3.5 nm. Targets include wake, oil, and floating objects. The background includes the sea at different times or in different situations. Prior target spectra are collected in advance from these targets in real scenes. A detailed description of the dataset is presented

in rows 2 to 4 of Table 2. The PI and GT for the dataset are presented in Figures 7A, B within rows 3 to 8.

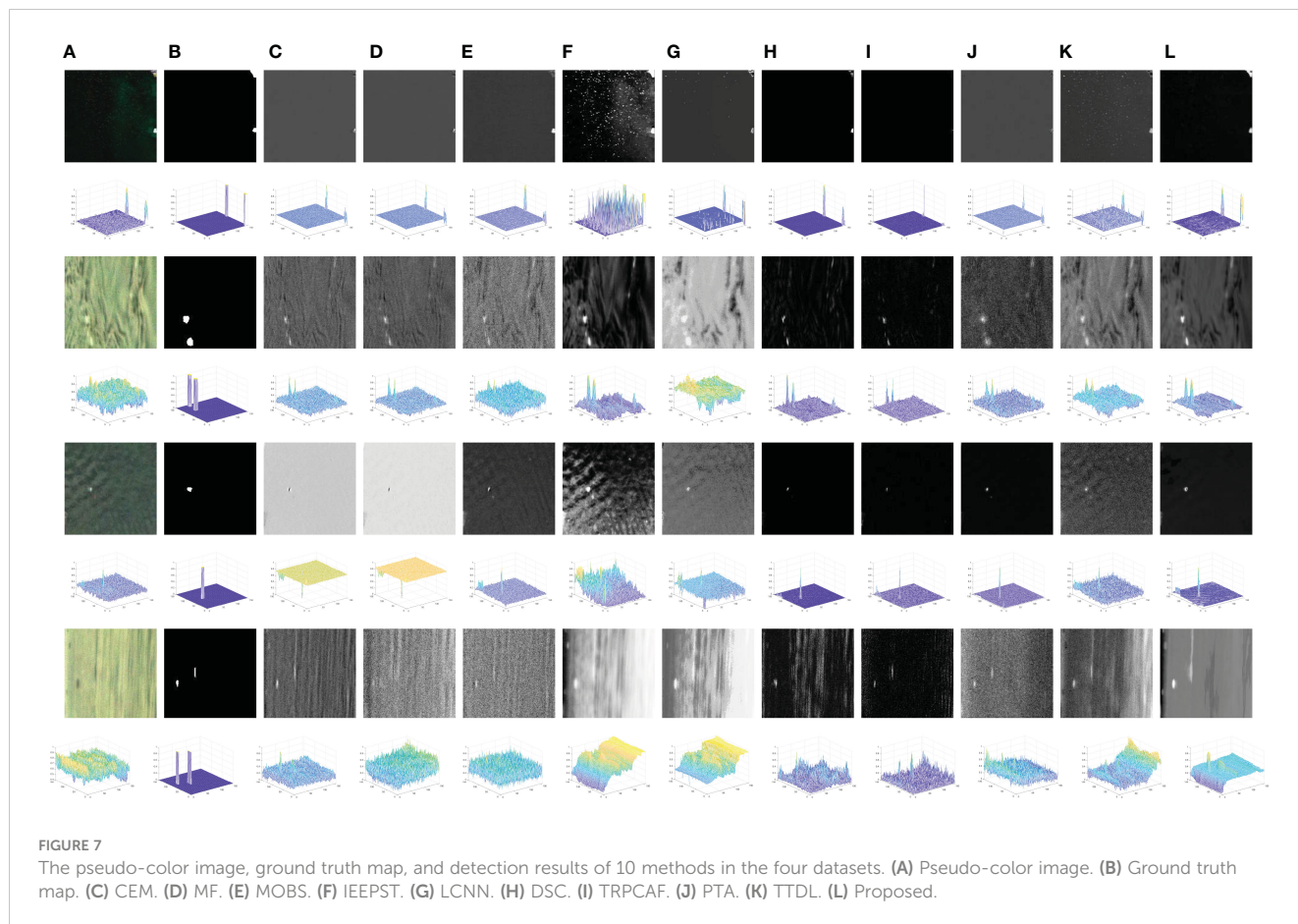
3.2 Evaluation indicators and analysis

To conduct qualitative and quantitative analyses, we used the detection result map, compared target-background separability, and introduced metrics such as detection probability (PD), false alarm probability (PF), and ROC.

Detection result maps are presented in grayscale, in which brighter shades indicate a proximity to the target. These maps provide a direct depiction of the target’s location. The algorithm’s performance is assessed based on the count of correct and erroneous pixels.

TABLE 2 Detailed description of the hyperspectral datasets.

Datasets	Collection date	Spectral resolution	Size (pixels)	Sensor
Ship	20/09/2012	5.0 ± 0.5nm	150×150×360	SpeTIR
Wake	01/02/2018	3.5 ± 0.5nm	150×150×176	GaiaSkymini2
Pollution	11/07/2018	3.5 ± 0.5nm	150×150×176	GaiaSkymini2
Floating object	01/02/2018	3.5 ± 0.5nm	150×155×176	GaiaSkymini2



In the box plot, the central line denotes the median value and the box's upper and lower edges denote 75% and 25% of the maximum values, respectively. The "whiskers" represent the extreme values of the detection results. The red box delineates the target value in detection results, whereas the green box delineates the background value in detection outcomes. The separation ability of the target background for the detection results is indicated by the distance between the green and red boxes (Hou et al., 2021). A larger distance signifies better algorithm performance.

Points on the ROC curve indicate the PDs at various PFs. The proximity of the ROC curve to top-left corner of the coordinate axis indicates superior detection results for the algorithm. PD quantifies the proportion of correctly detected pixels relative to the overall count of target pixels. PF denotes the proportion of background pixels erroneously classified as targets relative to the background pixel count (Li et al., 2021, 2022b). At a given PF value, higher PD values signify better algorithm performance (Zhao et al., 2022; Liu et al., 2023; Ge et al., 2024). The PD and PF can be calculated by Equations 44, 45:

$$PD = \frac{N_d}{N_t}, \tag{44}$$

$$PF = \frac{N_f}{N_b}, \tag{45}$$

where N_d , N_t , N_f , and N_b represent the number of correctly detected pixels, actual target pixels, pixels erroneously detected, and background pixels in the image, respectively. After getting an array corresponding to the PD and PF, the AUC is displayed as Equation 46:

$$AUC = \frac{1}{2} \times \sum_i^{mn} (PF_i - PF_{i-1}) \times (PD_i + PD_{i-1}), \tag{46}$$

where mn denotes the number of thresholds, $i \in 1, 2, \dots, mn$.

3.3 Detection performance

The parameters in this experiment encompass λ and β . In the spatial dimensionality unfolding of data, the value of λ is $1/\sqrt{T_2 T_3 \times T_1}$ or $1/\sqrt{T_1 T_3 \times T_2}$. In the spectral dimensionality unfolding of data, the value of λ is $1/\sqrt{T_1 T_2 \times T_3}$, and the value of β range is $[10^1, 10^2, 10^3, 10^4, 10^5]$. It is found through experiments that these two parameters have little effect on the experimental results, and the value of β used in this experiment was 10^1 . T_1, T_2

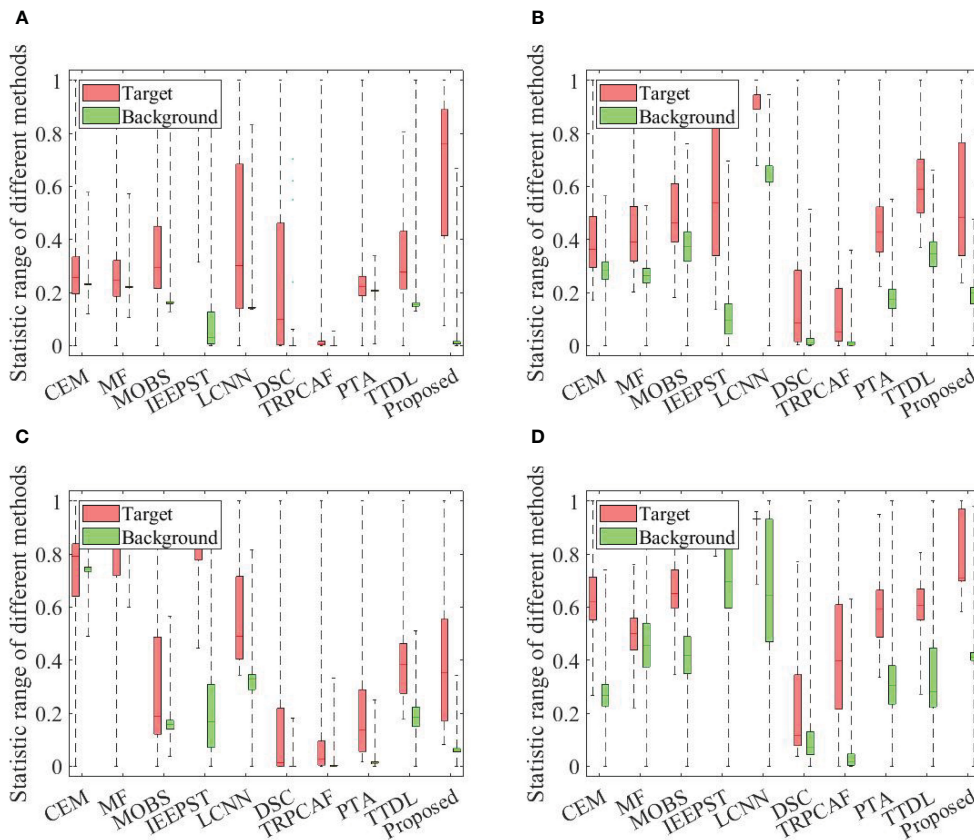


FIGURE 8 Statistical separability analysis of 10 methods in the four datasets. (A) Ship. (B) Wake. (C) Pollution. (D) Floating object.

and T_3 represent the rows, columns, and bands for the hyperspectral image, respectively. The comparison algorithms used in this study were as follows: CEM (Farrand and Harsanyi, 1997), MF (Manolakis et al., 2009), MOBS (Sun et al., 2024b), IEEPST (Sun et al., 2024c), LCNN (Dong et al., 2023), DSC (Zhang et al., 2020), TRPCAF (Chen and Wang, 2019), and PTA (Li et al., 2020), TTDL (Zhao et al., 2020a).

Figure 7 visually depicts the detection results using different algorithms across the four datasets. The proposed TRSSF algorithm demonstrates superior detection capability, identifying more target pixels across these datasets with minimal false alarms. In contrast, other comparison methods exhibit poor detection results. In rows 1 and 2 (Figure 7I), TRPCAF can barely detect the target. In rows 1 and 2 (Figures 7C–E, H, J), CEM, MF, MOBS, DSC, and PTA identify some correct pixels. In rows 1 and 2 (Figures 7F, G, K), IEEPST, LCNN, and TTDL can detect more target pixels but some error pixels are also detected. In rows 3 and 4 (h) and (i) of Figure 7, DSC and TRPCAF detect very few correct pixels. In rows 3 and 4 (Figures 7C–G, J, K), CEM, MF, MOBS, IEEPST, LCNN, PTA, and TTDL identify more correct pixels, albeit with numerous erroneous background pixels also detected. In rows 5 and 6 (Figures 7C–G, J, K), CEM, MF, DSC, TRPCAF, and PTA detect fewer correct pixels.

In rows 5 and 6 (Figures 7E–G, K), MOBS, IEEPST, LCNN, and TTDL can check more target pixels but also identify numerous false positives. In rows 7 and 8 (Figure 7I), TRPCAF detect fewer correct pixels. In rows 7 and 8 (Figures 7C–H, J, K), CEM, MF, MOBS, IEEPST, LCNN, DSC, PTA, and TTDL can identify more target pixels but also identify numerous false positives. Therefore, the proposed TRSSF has good detection performance.

Figure 8 shows a box plot diagram comparing the detection results across the four datasets using different methods. In Figure 8B, the green and red boxes' distance of LCNN and IEEPST are greater than the proposed TRSSF algorithm. In Figure 8C, the green and red boxes' distance of IEEPST is greater than the proposed TRSSF algorithm. However, the red and green boxes' distance in TRSSF are greater than those with the other algorithms. In Figures 8A, D, the green and red boxes separation of the TRSSF algorithm is greater those of the other algorithms, which can easily obtain the desired target from the images. Some of the remaining algorithms even have a partial overlap in the green and red boxes of the detection results. Therefore, the TRSSF's separation is better.

Figure 9 displays the ROC for various algorithms used to detect the results across the four datasets. In Figure 9A, when

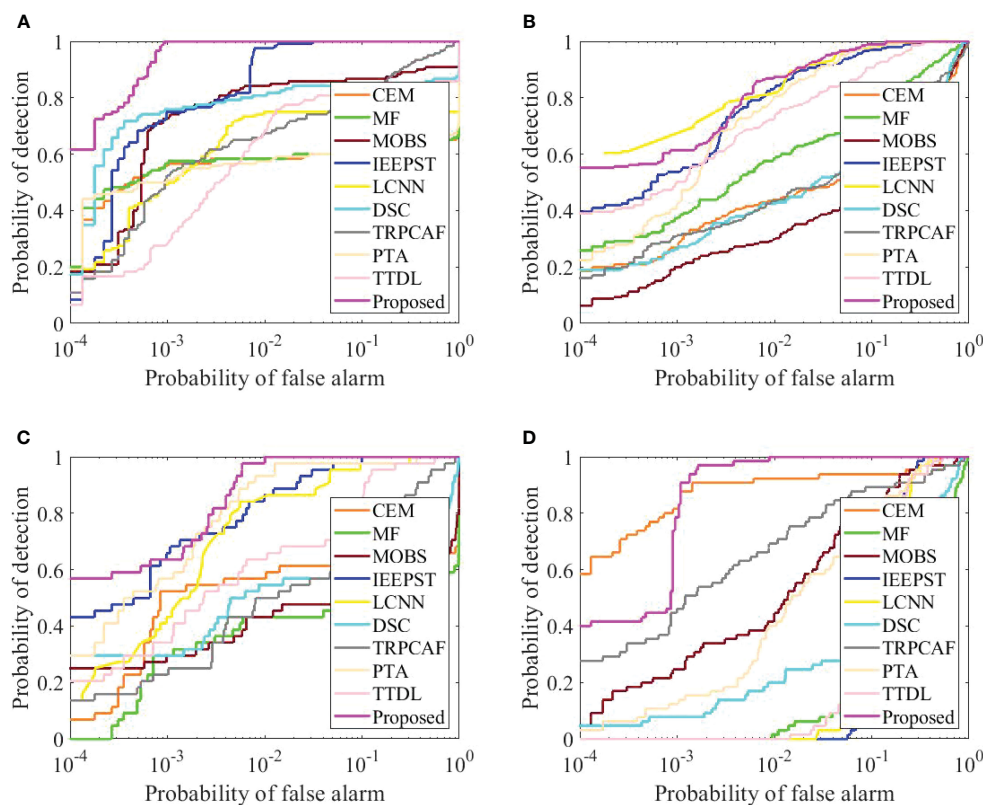


FIGURE 9 The ROC curve with different datasets. (A) Ship. (B) Wake. (C) Pollution. (D) Floating object.

TABLE 3 AUC values of different methods on four datasets.

Image	CEM	MF	MOBS	IEEPST	LCNN	DSC	TRPCAF	PTA	TTDL	Proposed
Ship	0.6338	0.6385	0.8948	0.9979	0.7490	0.8556	0.9241	0.6472	0.8431	0.9998
Wake	0.7832	0.9020	0.7539	0.9876	0.9908	0.7989	0.8235	0.9898	0.9728	0.9934
Pollution	0.6534	0.5518	0.5994	0.9935	0.9856	0.7120	0.8692	0.9898	0.9573	0.9986
Floating object	0.9756	0.6208	0.9374	0.8440	0.7957	0.7179	0.9376	0.9374	0.8615	0.9993

TABLE 4 Execution time of different methods on four datasets (unit: s).

Image	CEM	MF	MOBS	IEEPST	LCNN	DSC	TRPCAF	PTA	TTDL	Proposed
Ship	0.2339	0.2944	27.0741	15.2673	39.5312	6.5724	9.4338	86.1928	8.9818	41.5543
Wake	0.0828	0.116	15.1249	9.5659	4.3388	6.9591	3.0757	49.0279	6.5166	20.3282
Pollution	0.0765	0.1332	17.0592	5.4641	3.8812	5.3499	3.1292	42.7094	6.6764	41.0718
Floating object	0.1348	0.1299	14.8006	17.792	12.8928	11.889	2.5724	51.9833	7.2435	21.6437

the PF was approximately 0.1, the corresponding PD for TRSSF was approximately 1.0000. The PD s for all comparative methods (CEM, MF, MOBS, IEEPST, LCNN, DSC, TRPCAF, PTA, and TTDL) were 0.6167, 0.6000, 0.8667, 1.0000, 0.7500, 0.8417, 0.8250, 0.6000, and 0.8167, respectively. In Figures 9B–D, when the PF s were all 0.1, the PD s for TRSSF were 0.9902, 1.0000, and 1.0000. The biggest PD s among other baseline methods were 0.9805, 1.0000, and 0.9231. The proposed method's ROC curves were consistently closest to the upper left of the coordinate axis. The efficacy of the TRSSF algorithm was confirmed through an evaluation using the aforementioned four hyperspectral datasets.

Table 3 presents the AUC values for the aforementioned ten algorithms. On four different datasets, the TRSSF's AUCs were 0.9998, 0.9934, 0.9986, and 0.9993, respectively. The maximum AUC values for all comparison algorithms across the four real scenarios were 0.9979, 0.9908, 0.9935, and 0.9376, respectively. The minimum AUC values for all comparison methods across the four real scenarios were 0.6338, 0.7539, 0.5518, and 0.6208, respectively. All of them were lower than the AUC value of the TRSSF. The TRSSF's detection performance is optimal.

Table 4 presents the execution times of all the methods in different datasets. The times consumed by TRSSF were 41.5543 s, 20.3282 s, 41.0718 s, and 21.6437 s. The longest time consumed by the other methods on these datasets were 86.1928 s, 49.0279 s, 42.7094 s, and 51.9833 s, respectively. The time consumed by PTA was the longest. The time consumed by TRSSF was more than the traditional methods but less than the spatial-spectral fusion methods. The proposed TRSSF not only exhibits excellent detection performance for complex scenes but also does not take long to execute. All algorithm tests were conducted using MATLAB on a computer with an Intel Core i7-8700 h CPU and 8GB of RAM.

4 Conclusion

This study proposed a tensor adaptive reconstruction cascade spatial-spectral fusion (TRSSF) method for marine pollutants detection. First, the position of the pixel with the highest degree of matching with the prior spectral curve was obtained. This position could obtain the prior spectrum of the subsequent matching detection. Second, the tensor decomposition and reconstruction method based on the total variation and prior constraint was processed to the initial hyperspectral image. In the spatial dimensionality unfolding of the data, the linear total variational RPCA method was employed to obtain its rank. In the spectral dimensionality unfolding of data, similarity regularization RPCA was employed to obtain its rank. The data were reconstructed according to an adaptively chosen rank. Finally, the spatial-spectral fusion method was used to select the optimal target from the reconstructed data. Experiments performed on publicly available and laboratory-collected hyperspectral datasets showcased the effective detection performance of the proposed approach.

In the future, as the application scenarios become more complex, the data will become increasingly larger. Too many bands in the hyperspectral data will result in the data containing a large amount of redundant information, which makes data processing and analysis more complicated and reduces the efficiency and detection rate of target detection. Therefore, hyperspectral target detection based on band selection will be the direction that will be studied in the next phase. At the same time, some existing hyperspectral moving targets have rich temporal information; therefore, the study of combining spatial and temporal information can further improve the target detection rate.

Data availability statement

The original contributions presented in the study are included in the article/supplementary material. Further inquiries can be directed to the corresponding author.

Author contributions

ZX: Writing – review & editing, Writing – original draft, Methodology, Funding acquisition, Data curation, Conceptualization. KG: Writing – review & editing. FH: Writing – review & editing. JC: Writing – review & editing. ZX: Writing – review & editing. LS: Writing – review & editing. ML: Writing – review & editing.

Funding

The author(s) declare financial support was received for the research, authorship, and/or publication of this article. This

References

- Akhter, M. A., Heylen, R., and Scheunders, P. (2014). A geometric matched filter for hyperspectral target detection and partial unmixing. *IEEE Geosci. Remote Sens. Lett.* 12, 661–665. doi: 10.1109/LGRS.2014.2355915
- Aptoula, E., Mura, M. D., and Lefèvre, S. (2016). Vector attribute profiles for hyperspectral image classification. *IEEE Trans. Geosci. Remote Sens.* 54, 3208–3220. doi: 10.1109/TGRS.2015.2513424
- Bao, R., Xia, J., Mura, M. D., Du, P., Chanussot, J., and Ren, J. (2016). Combining morphological attribute profiles via an ensemble method for hyperspectral image classification. *IEEE Geosci. Remote Sens. Lett.* 13, 359–363. doi: 10.1109/LGRS.2015.2513002
- Cai, J., Candès, E., and Shen, Z. (2010). A singular value thresholding algorithm for matrix completion. *SIAM J. Optim.* 20, 1956–1982. doi: 10.1137/080738970
- Candès, E. J., Li, X., Ma, Y., and Wright, J. (2011). Robust principal component analysis. *J. ACM* 58, 1–37. doi: 10.1145/1970392.1970395
- Chang, C. (1999). “Spectral information divergence for hyperspectral image analysis,” in *IEEE 1999 International Geoscience and Remote Sensing Symposium. IGARSS’99 (Cat. No. 99CH36293)*, Hamburg, Germany: IEEE Vol. 1. 509–511. doi: 10.1109/IGARSS.1999.773549
- Chen, X., Zhang, M., and Liu, Y. (2024). Target detection with spectral graph contrast clustering assignment and spectral graph transformer in hyperspectral imagery. *IEEE Trans. Geosci. Remote Sens.* 62, 1–16. doi: 10.1109/TGRS.2024.3394616
- Chen, Y., Nasrabadi, N., and Tran, T. (2011). Sparse representation for target detection in hyperspectral imagery. *IEEE J. Sel. Top. Signal Process.* 5, 629–640. doi: 10.1109/JSTSP.2011.2113170
- Chen, Z., and Wang, B. (2019). Hyperspectral target detection based on tensor sparse representation. *IEEE Geosci. Remote Sens. Lett.* 16, 1605–1609. doi: 10.1109/LGRS.8859
- Chen, Z., Yang, B., and Wang, B. (2018). A preprocessing method for hyperspectral target detection based on tensor principal component analysis. *Remote Sens.* 10, 1033–1053. doi: 10.3390/rs10071033
- Coorey, R. (2018). “The evolution of geospatial intelligence,” in *Australian contributions to strategic and military geography*, Midtown Manhattan, New York, USA: Springer 143–151.
- Dian, R., Fang, L., and Li, S. (2017). “Hyperspectral image super-resolution via non-local sparse tensor factorization,” in *Proceedings of the IEEE conference on computer vision and pattern recognition*, Honolulu, Hawaii: IEEE 5344–5353. doi: 10.1109/CVPR.2017.411
- DiPietro, R. S., Manolakis, D. G., Lockwood, R. B., Cooley, T., and Jacobson, J. (2012). Hyperspectral matched filter with false-alarm mitigation. *Opt. Eng.* 51, 016202–016202. doi: 10.1117/1.OE.51.1.016202
- Dong, Y., Dai, X., Zhang, Y., and Du, B. (2023). A lightweight convolutional neural network based on joint correlation distance constraints and density peak clustering for

research was partly supported by the Postdoctoral Science Foundation of China under Grant 2023M740240 and partly supported by the Open Project of Fujian Key Laboratory of Spatial Information Perception and Intelligent Processing (Yango University, Grant No. FKLSIPIP1018).

Conflict of interest

The authors declare that the research was conducted in the absence of any commercial or financial relationships that could be construed as a potential conflict of interest.

Publisher’s note

All claims expressed in this article are solely those of the authors and do not necessarily represent those of their affiliated organizations, or those of the publisher, the editors and the reviewers. Any product that may be evaluated in this article, or claim that may be made by its manufacturer, is not guaranteed or endorsed by the publisher.

hyperspectral target detection. *IEEE Trans. Geosci. Remote Sens.* 61, 1–14. doi: 10.1109/TGRS.2023.3292292

Dong, W., Wu, X., Qu, J., Gamba, P., Xiao, S., Vizziello, A., et al. (2024). Deep spatial-spectral joint-sparse prior encoding network for hyperspectral target detection. *IEEE Trans. Cybern.* 54, 1–13. doi: 10.1109/TCYB.2024.3403729

Du, B., and Zhang, L. (2010). Random-selection-based anomaly detector for hyperspectral imagery. *IEEE Trans. Geosci. Remote Sens.* 49, 1578–1589. doi: 10.1109/TGRS.2010.2081677

Farrand, W. H., and Harsanyi, J. C. (1997). Mapping the distribution of mine tailings in the coeur d’alene river valley, idaho, through the use of a constrained energy minimization technique. *Remote Sens. Environ.* 59, 64–76. doi: 10.1016/S0034-4257(96)00080-6

Feng, S., Tang, S., Zhao, C., and Cui, Y. (2021). A hyperspectral anomaly detection method based on low-rank and sparse decomposition with density peak guided collaborative representation. *IEEE Trans. Geosci. Remote Sens.* 60, 1–13. doi: 10.1109/TGRS.2021.3054736

Gao, L., Wang, D., Zhuang, L., Sun, X., Huang, M., and Plaza, A. (2023). BS³Net: A new blind-spot self-supervised learning network for hyperspectral anomaly detection. *IEEE Trans. Geosci. Remote Sens.* 61, 1–18. doi: 10.1109/TGRS.2023.3246565

Ge, F., Xuan, K., Lou, P., Li, J., Jiang, L., Wang, J., et al. (2024). Multi-object detection and behavior tracking of sea cucumbers with skin ulceration syndrome based on deep learning. *Front. Mar. Sci.* 11, 1365155. doi: 10.3389/fmars.2024.1365155

Giannandrea, A., Raqueno, N., Messinger, D. W., Faulring, J., Kerekes, J. P., Van Aardt, J., et al. (2013). “The share 2012 data campaign,” in *Algorithms and technologies for multispectral, hyperspectral, and ultraspectral imagery XIX*, vol. 8743. (Baltimore, Maryland, United States: SPIE), 94–108. doi: 10.1117/12.2015935

Guo, X., Huang, X., Zhang, L., and Zhang, L. (2013). Hyperspectral image noise reduction based on rank-1 tensor decomposition. *ISPRS J. Photogramm. Remote Sens.* 83, 50–63. doi: 10.1016/j.isprsjprs.2013.06.001

Harsanyi, J. C., and Chang, C.-I. (1994). Hyperspectral image classification and dimensionality reduction: An orthogonal subspace projection approach. *IEEE Trans. Geosci. Remote Sens.* 32, 779–785. doi: 10.1109/36.298007

He, R., Hu, B., Zheng, W., and Kong, X. (2011). Robust principal component analysis based on maximum correntropy criterion. *IEEE Trans. Image Process.* 20, 1485–1494. doi: 10.1109/TIP.2010.2103949

He, W., Zhang, H., Zhang, L., and Shen, H. (2015). Total variation regularized low-rank matrix factorization for hyperspectral image restoration. *IEEE Trans. Geosci. Remote Sens.* 54, 178–188. doi: 10.1109/TGRS.2015.2452812

Hou, Z., Li, W., Li, L., Tao, R., and Du, Q. (2021). Hyperspectral change detection based on multiple morphological profiles. *IEEE Trans. Geosci. Remote Sens.* 60, 1–12. doi: 10.1109/TGRS.2021.3090802

- Hou, Z., Li, W., Tao, R., Ma, P., and Shi, W. (2022). Collaborative representation with background purification and saliency weight for hyperspectral anomaly detection. *Sci. China Inf. Sci.* 65, 1–12. doi: 10.1007/s11432-020-2915-2
- Kang, Z., Peng, C., and Cheng, Q. (2015). "Robust pca via nonconvex rank approximation," in *2015 IEEE International Conference on Data Mining*. 211–220 (Atlantic City, NJ, USA: IEEE). doi: 10.1109/ICDM.2015.15
- Kolda, T., and Bader, B. (2009). Tensor decompositions and applications. *SIAM Rev.* 51, 455–500. doi: 10.1137/07070111X
- Kruse, F. A., Lefkoff, A., Boardman, J., Heidebrecht, K., Shapiro, A., Barloon, P., et al. (1993). The spectral image processing system (sips)—interactive visualization and analysis of imaging spectrometer data. *Remote Sens. Environ.* 44, 145–163. doi: 10.1016/0034-4257(93)90013-N
- Li, S., Dian, R., Fang, L., and Bioucas-Dias, J. (2018). Fusing hyperspectral and multispectral images via coupled sparse tensor factorization. *IEEE Trans. Image Process.* 27, 4118–4130. doi: 10.1109/TIP.2018.2836307
- Li, W., and Du, Q. (2016). A survey on representation-based classification and detection in hyperspectral remote sensing imagery. *Pattern Recognit. Lett.* 83, 115–123. doi: 10.1016/j.patrec.2015.09.010
- Li, L., Li, W., Qu, Y., Zhao, C., Tao, R., and Du, Q. (2020). Prior-based tensor approximation for anomaly detection in hyperspectral imagery. *IEEE Trans. Neural Netw. Learn Syst.* 33, 1037–1050. doi: 10.1109/TNNLS.2020.3038659
- Li, L., Ma, H., and Jia, Z. (2021). Change detection from SAR images based on convolutional neural networks guided by saliency enhancement. *Remote Sens.* 13, 3697–3717. doi: 10.3390/rs13183697
- Li, L., Ma, H., and Jia, Z. (2022b). Multiscale geometric analysis fusion-based unsupervised change detection in remote sensing images via flicm model. *Entropy* 24, 291. doi: 10.3390/e24020291
- Li, J., Zheng, K., Gao, L., Ni, L., Huang, M., and Chanussot, J. (2024). Model-informed multistage unsupervised network for hyperspectral image super-resolution. *IEEE Trans. Geosci. Remote Sens.* 62, 1–17. doi: 10.1109/TGRS.2024.3391014
- Li, J., Zheng, K., Li, Z., Gao, L., and Jia, X. (2023a). X-shaped interactive autoencoders with crossmodality mutual learning for unsupervised hyperspectral image super-resolution. *IEEE Trans. Geosci. Remote Sens.* 61, 1–17. doi: 10.1109/TGRS.2023.3300043
- Li, J., Zheng, K., Liu, W., Li, Z., Yu, H., and Ni, L. (2023b). Model-guided coarse-to-fine fusion network for unsupervised hyperspectral image super-resolution. *IEEE Geosci. Remote Sens. Lett.* 20, 1–5. doi: 10.1109/LGRS.2023.3309854
- Li, J., Zheng, K., Yao, J., Gao, L., and Hong, D. (2022a). Deep unsupervised blind hyperspectral and multispectral data fusion. *IEEE Geosci. Remote Sens. Lett.* 19, 1–5. doi: 10.1109/LGRS.2022.3151779
- Liu, Y., Gao, G., and Gu, Y. (2016). Tensor matched subspace detector for hyperspectral target detection. *IEEE Trans. Geosci. Remote Sens.* 55, 1967–1974. doi: 10.1109/TGRS.2016.2632863
- Liu, J., Hou, Z., Li, W., Tao, R., Orlando, D., and Li, H. (2021a). Multipixel anomaly detection with unknown patterns for hyperspectral imagery. *IEEE Trans. Neural Netw. Learn Syst.* 33, 5557–5567. doi: 10.1109/TNNLS.2021.3071026
- Liu, M., Jiang, W., Hou, M., Qi, Z., Li, R., and Zhang, C. (2023). A deep learning approach for object detection of rockfish in challenging underwater environments. *Front. Mar. Sci.* 10, 1242041. doi: 10.3389/fmars.2023.1242041
- Liu, N., Li, L., Li, W., Tao, R., Fowler, J. E., and Chanussot, J. (2021b). Hyperspectral restoration and fusion with multispectral imagery via low-rank tensor-approximation. *IEEE Trans. Geosci. Remote Sens.* 59, 7817–7830. doi: 10.1109/TGRS.2020.3049014
- Manolakis, D., Lockwood, R., Cooley, T., and Jacobson, J. (2009). "Is there a best hyperspectral detection algorithm?," in *Algorithms and technologies for multispectral, hyperspectral, and ultraspectral imagery XV*, Orlando, Florida, United States: SPIE vol. 7334, 13–28. doi: 10.1117/12.816917
- Manolakis, D., Marden, D., and Shaw, G. (2003). Hyperspectral image processing for automatic target detection applications. *Linc Lab. J.* 14, 79–116.
- Nasrabadi, N. (2013). Hyperspectral target detection: An overview of current and future challenges. *IEEE Signal Process. Mag.* 31, 34–44. doi: 10.1109/MSP.2013.2278992
- Renard, N., and Bourennane, S. (2008). Improvement of target detection methods by multiway filtering. *IEEE Trans. Geosci. Remote Sens.* 46, 2407–2417. doi: 10.1109/TGRS.2008.918419
- Renard, N., and Bourennane, S. (2009). Dimensionality reduction based on tensor modeling for classification methods. *IEEE Trans. Geosci. Remote Sens.* 47, 1123–1131. doi: 10.1109/TGRS.2008.2008903
- Shi, W., Li, J., Zheng, Y., Xi, B., and Li, Y. (2020). Hyperspectral target detection with roi feature transformation and multiscale spectral attention. *IEEE Trans. Geosci. Remote Sens.* 59, 5071–5084. doi: 10.1109/TGRS.2020.3001948
- Sun, X., Lin, P., Shang, X., Pang, H., and Fu, X. (2024b). Mobs-td: Multiobjective band selection with ideal solution optimization strategy for hyperspectral target detection. *IEEE J. Sel. Top. Appl. Earth Obs. Remote Sens.* 17, 10032–10050. doi: 10.1109/JSTARS.2024.3402381
- Sun, L., Ma, Z., and Zhang, Y. (2024a). Ablal: Adaptive background latent space adversarial learning algorithm for hyperspectral target detection. *IEEE J. Sel. Top. Appl. Earth Obs. Remote Sens.* 17, 411–427. doi: 10.1109/JSTARS.2023.3329771
- Sun, X., Qu, Y., Gao, L., Sun, X., Qi, H., Zhang, B., et al. (2020). Target detection through tree-structured encoding for hyperspectral images. *IEEE Trans. Geosci. Remote Sens.* 59, 4233–4249. doi: 10.1109/TGRS.2020.3024852
- Sun, X., Zhuang, L., Gao, L., Gao, H., Sun, X., and Zhang, B. (2024c). A point-set topology-based information entropy estimation method for hyperspectral target detection. *IEEE Trans. Geosci. Remote Sens.* 62, 1–17. doi: 10.1109/TGRS.2024.3400321
- Veganzones, M., Cohen, J., Farias, R., Chanussot, J., and Comon, P. (2015). Nonnegative tensor cp decomposition of hyperspectral data. *IEEE Trans. Geosci. Remote Sens.* 54, 2577–2588. doi: 10.1109/TGRS.2015.2503737
- Wang, D., Zhuang, L., Gao, L., Sun, X., Huang, M., and Plaza, A. (2023). Pdbnsnet: Pixel-shuffle downsampling blind-spot reconstruction network for hyperspectral anomaly detection. *IEEE Trans. Geosci. Remote Sens.* 61, 1–14. doi: 10.1109/TGRS.2023.3276175
- Wang, D., Zhuang, L., Gao, L., Sun, X., Zhao, X., and Plaza, A. (2024). Sliding dual-window-inspired reconstruction network for hyperspectral anomaly detection. *IEEE Trans. Geosci. Remote Sens.* 62, 1–15. doi: 10.1109/TGRS.2024.3351179
- Wei, Y., Niu, C., Wang, Y., Wang, H., and Liu, D. (2019). The fast spectral clustering based on spatial information for large scale hyperspectral image. *IEEE Access* 7, 141045–141054. doi: 10.1109/Access.6287639
- Xu, Y., Wu, Z., Chanussot, J., Comon, P., and Wei, Z. (2019). Nonlocal coupled tensor cp decomposition for hyperspectral and multispectral image fusion. *IEEE Trans. Geosci. Remote Sens.* 58, 348–362. doi: 10.1109/TGRS.36
- Yang, X., Chen, J., and He, Z. (2019). Sparse-spatialcsm for hyperspectral target detection. *IEEE J. Sel. Top. Appl. Earth Obs. Remote Sens.* 12, 2184–2195. doi: 10.1109/JSTARS.4609443
- Yang, S., and Shi, Z. (2016). Hyperspectral image target detection improvement based on total variation. *IEEE Trans. Image Process* 25, 2249–2258. doi: 10.1109/TIP.2016.2545248
- Zhang, G., Zhao, S., Li, W., Du, Q., Ran, Q., and Tao, R. (2020). Htd-net: A deep convolutional neural network for target detection in hyperspectral imagery. *Remote Sens.* 12, 1489. doi: 10.3390/rs12091489
- Zhao, X., Hou, Z., Wu, X., Li, W., Ma, P., and Tao, R. (2021b). Hyperspectral target detection based on transform domain adaptive constrained energy minimization. *Int. J. Appl. Earth Obs. Geoinf.* 103, 102461. doi: 10.1016/j.jag.2021.102461
- Zhao, M., Li, W., Li, L., Ma, P., Cai, Z., and Tao, R. (2021a). Three-order tensor creation and Tucker decomposition for infrared small-target detection. *IEEE Trans. Geosci. Remote Sens.* 60, 1–16. doi: 10.1109/TGRS.2021.3057696
- Zhao, X., Li, W., Shan, T., Li, L., and Tao, R. (2020b). "Hyperspectral target detection by fractional Fourier transform," in *IGARSS 2020-2020 IEEE International Geoscience and Remote Sensing Symposium*. 1655–1658 (Waikoloa, HI, USA: IEEE). doi: 10.1109/IGARSS39084.2020
- Zhao, X., Li, W., Zhang, M., Tao, R., and Ma, P. (2020c). Adaptive iterated shrinkage thresholding-based lp-norm sparse representation for hyperspectral imagery target detection. *Remote Sens.* 12, 3991. doi: 10.3390/rs12233991
- Zhao, X., Li, W., Zhao, C., and Tao, R. (2022). Hyperspectral target detection based on weighted Cauchy distance graph and local adaptive collaborative representation. *IEEE Trans. Geosci. Remote Sens.* 60, 1–13. doi: 10.1109/TGRS.2022.3169171
- Zhao, X., Liu, K., Gao, K., and Li, W. (2023). Hyperspectral time-series target detection based on spectral perception and spatial-temporal tensor decomposition. *IEEE Trans. Geosci. Remote Sens.* 60, 1–12. doi: 10.1109/TGRS.2023.3307071
- Zhao, C., Wang, M., Su, N., and Feng, S. (2020a). "Dictionary learning hyperspectral target detection algorithm based on Tucker tensor decomposition," in *IGARSS 2020-2020 IEEE International Geoscience and Remote Sensing Symposium*. Waikoloa, HI, USA: IEEE 1763–1766. doi: 10.1109/IGARSS39084.2020.9324144
- Zou, Z., and Shi, Z. (2015). Hierarchical suppression method for hyperspectral target detection. *IEEE Trans. Geosci. Remote Sens.* 54, 330–342. doi: 10.1109/TGRS.2015.2456957